INFLUENCE OF TEMPERING TIME ON THE FRACTURE TOUGHNESS OF HYDROGEN PRE-CHARGED 42CrMo4 STEEL

A. Zafra[1], G. Álvarez[1], J. Belzunce[1*] and C. Rodríguez[1]

[1]SIMUMECAMAT research group, University of Oviedo, Polytechnic School of Engineering, 33203, Gijón, Asturias, Spain

[*]Corresponding author: belzunce@uniovi.es

ABSTRACT

This work aims to find suitable 42CrMo4 steel grades for working in energetic applications dealing with high pressure hydrogen gas. Consequently, the influence of the tempering time on the hydrogen embrittlement (HE) sensitivity of 42CrMo4 steel quenched and tempered at 600ºC is studied. Compact tension (CT) specimens were pre-charged with gaseous hydrogen in a pressurized reactor at 19.5 MPa and 450ºC for 21 hours and tested for fracture toughness afterwards in air. The hydrogen concentration introduced in the steels was determined using thermal desorption analysis (TDA). The fracture micromechanisms were subsequently identified by means of scanning electron microscopy (SEM). Electrochemical hydrogen permeation (EHP) tests were also performed to gain better insight into the interaction between hydrogen atoms and the microstructure of these steel grades, and consequently to justify the results. The fracture toughness of hydrogenated 42CrMo4 steel increases considerably with the tempering time, being this behaviour correlated with the hydrogen trapping capability of the steel. Brittle fracture micromechanisms, associated with the hydrogen-enhanced decohesion mechanism HEDE (martensitic lath decohesion and intergranular fracture) were present to a lesser or greater degree in all the tempering times.

KEYWORDS: Hydrogen embrittlement, fracture toughness, diffusion, tempering time, fracture micromechanisms.

1. INTRODUCTION

The growing importance of hydrogen energy in the global energy landscape requires the development of economical steels able to safely transport large amounts of pressurized hydrogen without suffering from hydrogen embrittlement.

Due to its small atomic size, hydrogen is easily absorbed in the BCC structure of steel when it is submitted to high pressures. In these conditions it is able to diffuse along the crystalline lattice of the steel, driven by stress and concentration gradients [1–3]. Eventually, hydrogen atoms are trapped into lattice imperfections such as vacancies, dislocations and internal interfaces, known as hydrogen traps [4,5]. These traps are characterized by their density, N_t, and binding energy, E_b. Large accumulations of hydrogen in these sites drastically modifies the steel failure micromechanisms when it is submitted to mechanical loads [6,7], leading to a deterioration of its mechanical properties.

The two most relevant hydrogen damage mechanisms in the case of quenched and tempered CrMo steels are the hydrogen-enhanced localised plasticity (HELP) and the hydrogen-enhanced decohesion (HEDE) [8]. However, although some authors have isolated the effects of these mechanisms [9], others claim that the independent occurrence of HELP or HEDE is frequently unable to explain hydrogen failures [10–12]. In fact, some works have reported that these mechanisms act in a synergistic interplay, known as HELP mediated HEDE [13,14]. In this case, hydrogen first facilitates dislocation mobility in highly strained areas (HELP), which fosters hydrogen accumulation in the process zone ahead of the crack tip. The local stress state is modified in this zone and the cohesive strength of internal interfaces is reduced (HEDE). The fracture surfaces are characterized by brittle features: decohesion along internal interfaces such as martensitic laths, or grain boundaries [9,14,15]. Nevertheless, despite decades of research into the mechanisms of hydrogen induced failure, there is still much controversy surrounding the identification and understanding of the failure mechanisms caused by HE in different materials in different conditions [16].

Based on the assumption that HE is governed by a combination of a defined amount of local accumulated hydrogen and critical stress levels [17–19], it is obvious that the interaction between hydrogen atoms and dislocations play an essential role in triggering this phenomenon. In CrMo steels with martensitic microstructures, the dislocation density is directly related to the hardness of the steel, i.e., its yield strength [20]. In addition, this mechanical property, determines the hydrostatic stress level in the crack tip when a load is applied, σ_H, and therefore the amount of hydrogen accumulated in this particular region, C_{Hloc}, Equation (1) [2].

$$C_{Hloc} = C_{H0} \cdot e^{\left(\sigma_H V_H / RT\right)} \quad (1)$$

where C_{H0} is the hydrogen present in the absence of stress, V_H is the partial molar volume of hydrogen in BCC iron (V_H=2.1 10^{-6} m^3/mol), R the gas constant and T is the temperature.

In this context, the development of heat treatments able to improve the HE resistance of martensitic CrMo steels, without compromising their strength, plays an essential role in the development of hydrogen storage and transport facilities, such as pressure vessels and pipes. Quenched and tempered CrMo or CrNiMo alloy steels are good candidates for these applications and, as the susceptibility of steels to embrittlement by gaseous hydrogen increases with increasing their mechanical strength, the steel ultimate tensile strength is limited to values lower than 950 MPa [21].

When vessels dimensions are large, these components may be made from welded plates and are usually submitted to a post-welding heat treatment (PWHT). Typically, in order to minimize HE of welded joints, CrMo and CrMoV steels are post-weld tempered at high temperatures, during which their strength and hardness significantly decline as shown, among other works, in [22–24]. In general, the application of tempering temperatures within the range of 650-720ºC for 2-10 hours provides the best mechanical behaviour under internal hydrogen. For example, Tvrdy et al. [25], demonstrated that even low-strength CrMo pressure vessel steels are susceptible to subcritical crack growth under stress intensity factor levels far below the critical fracture toughness value of the corresponding steel, $K_{IC.}$ They showed that the resistance to HE of their welds (hardened microstructures with higher dislocation density) increases considerably after tempering at the maximum possible temperature. In fact, Mitchell et al. [22] studied the optimisation of the PWHT in a 1.25Cr0.5Mo pressure vessel steel to be used in a high temperature hydrogen service and suggested that tempering in the range of 670º-710ºC for 8 hours could be the optimal solution for resistance to HE. Similarly, Dai and Lippold [23], propose a PWHT of 660ºC/10h as optimal for reducing hydrogen-assisted cracking of the CGHAZ in 2.25Cr1Mo steels.

Regarding 42CrMo4 steel, although this kind of data is scarce, the influence of the tempering temperature on the fracture toughness of hydrogen pre-charged samples was assessed in a previous work by this research group [26]. It was reported that the lowest fracture toughness reduction took place when the steel was tempered at the highest temperature, 700ºC. However, in that work, the tempering time was always two hours, and the influence of this variable was not evaluated. The interchangeability of time and temperature is usually accomplished by use of the Hollomon-Jaffe tempering parameter, P:

$$P = T\left(20 + log(t)\right) \quad (2)$$

where T is the temperature in K and t is the time in hours, but the application of this parameter to explain HE phenomena on steels needs further research.

Consequently, the aim of this paper is to study the influence of internal hydrogen on the fracture toughness of 42CrMo4 steel quenched and tempered at 600ºC for different times (30 min, 2h, 24h and 7d). A tempering temperature of 600ºC was selected with the objective of attaining full tempered microstructures with relatively low strength and high ductility and toughness after long time treatments and, on the contrary, low tempered and high strength grades with lower toughness when low tempering times are applied. A very long, but impractical, tempering time was also included (7d) to evaluate if it was able to provide a significant improvement in the steel's HE resistance. A comprehensive analysis of the fracture surfaces is carried out in order to identify the main fracture micromechanisms and to establish the HE mechanisms that take place during the mechanical tests. These results

are supported by hydrogen content measurements and electrochemical permeation tests, which make it possible to determine the apparent hydrogen diffusion coefficient, D_{app}, of the studied grades and to estimate the trapping capability of the steels.

2. EXPERIMENTAL PROCEDURE

2.1 Material and heat treatments

Hot rolled plates of 250x125x12 mm of commercial 42CrMo4 steel (0.42%C, 0.98%Cr, 0.22%Mo) were austenitized at 845ºC for 40 min, quenched in still water, and tempered at 600ºC for different times: 30 minutes, 2 hours, 24 hours, and 7 days. In order to assess the influence of tempering time on HE, fracture toughness tests were performed on hydrogen pre-charged compact tension (CT) specimens machined on these 4 grades, which were designated according to their tempering time. Microstructural and mechanical characterization were performed using scanning electron microscopy (SEM JEOL-JSM5600), hardness *HV30* measurements and tensile tests on standard specimens (Ø=5mm).

2.2 Hydrogen pre-charge

The fracture toughness CT specimens of the four grades were hydrogen pre-charged at 450ºC for 21 hours in a reactor containing hydrogen gas at 19.5 MPa. Although a theoretical hydrogen content of 4.1 wppm is attained under the aforementioned charging conditions [26] - at this relatively high temperature, microstructural traps are not active and hydrogen saturation can be considered to be the same than in pure BCC iron -, important hydrogen losses take always place during the cooling stage needed before extracting the specimens from the reactor. After hydrogen pre-charging, the specimens were maintained at cryogenic temperatures (in liquid nitrogen) until the moment of testing in order to avoid further hydrogen losses. In order to measure the real amount of hydrogen present in the steels at the beginning of the fracture toughness tests, cylindrical samples (with a length of 30 mm and a diameter of 10 mm) were pre-charged under the same conditions. Their total hydrogen content was measured by means of thermal desorption analysis (TDA) in a Leco DH603. The hydrogen desorption curves were also determined to ensure that enough hydrogen content was kept in the samples during the mechanical tests. More details on hydrogen charging and hydrogen content measurements are provided in [26,27].

2.3 Hydrogen permeation tests

With the aim of correlating the fracture toughness properties in presence of internal hydrogen with the apparent hydrogen diffusion coefficient of the steels, D_{app}, electrochemical permeation tests were performed. This is especially relevant because D_{app} is a good indicator of the density of trapping sites [28]. Single-transient permeation tests were carried out in a double-cell following the ASTM G148 [29] standard. Flat specimens with a thickness between 0.8 and 1 mm (ground to 1200 grit) were used, and a circular area of 1.25 cm^2 was exposed to both cells.

The cathodic cell was filled with 1M H_2SO_4 + 0.25 g/l As_2O_3 (to avoid recombination of hydrogen atoms) and hydrogen was generated by applying a constant cathodic current density, J_c, of 0.5 mA/cm^2 between the specimen and a platinum counter electrode. As D_{app} is dependent on the hydrogen concentration in the steel [30,31], in this work a low current value was chosen to characterize hydrogen diffusivity under low trap occupancy levels. This situation is expected after the important hydrogen losses that take place during the cooling phase after gaseous charging. In addition, a low J_c value minimizes the likelihood of surface damage and hydrogen recombination. The anodic cell was filled with 0.1MNaOH, where hydrogen atoms were oxidated and a permeation current, J_p, recorded vs. time using a PalmSense4 potentiostat. In order to avoid the oxidation of other species, a thin palladium coating (≈50-100 nm) was electrodeposited on the anodic surface of the sample prior to testing. The anodic face was polarized at a constant potential of 40-50 mV vs. Ag/AgCl reference electrode to ensure an initial permeation background density below 0.1 $\mu A/cm^2$.

At the end of the test, the D_{app} value was calculated from the permeation transient using the t_{lag} method, as indicated in [29]. Two permeation tests were performed for each grade, so the mean value and the average standard deviation are provided.

2.4 Fracture toughness tests

Fracture toughness tests were performed on CT specimens with a width, *W*, of 48 mm, a thickness, *B*, of 12 mm, and an initial notch, a_n, of 20 mm. Firstly, the specimens were fatigue pre-cracked under a load ratio, *R*, of 0.1 and a frequency, *f*, of 10 Hz, until reaching a crack length versus width ratio, *a/W*, of 0.5 (a_0=25 mm), as indicated in the ASTM E1820 standard [32]. Next, lateral notches were machined on both sides of the specimen to obtain a net thickness, B_n, of 10 mm, so as to assure a plane strain state.

These tests were carried out in a servohydraulic universal MTS testing machine provided with a load cell of 100 kN. The crack growth throughout the test was determined by means of the compliance method using a COD gauge and performing partial discharges (25%). The value of J obtained in each discharge was determined as the sum of its elastic and plastic component. The former was calculated from the stress intensity factor, *K*, and the latter was obtained by integrating the area below the Load-Load Line Displacement (*P-LLD*) plot, following the procedure described in [32].

After the test, the initial, a_0, and final, a_f, crack lengths were corrected by measuring them onto the fracture surface of the broken specimens. Consequently, the fracture toughness-crack growth (J-Δa) curves were obtained and the fracture toughness parameter, $J_{0.2/BL}$ (in kJ/m^2), was determined. This parameter corresponds to the value of *J* after an effective crack growth of 0.2 mm regarding the blunting of the crack tip and was employed to assess the fracture toughness for the onset of crack growth. The slope of the blunting line was determined using Equation 3, where σ_{ys} and σ_{ut} are the yield and ultimate strengths respectively [32].

$$\frac{J}{\Delta a} = 2\left(\frac{\sigma_{ys} + \sigma_{uts}}{2}\right) \quad (3)$$

In order to assess the influence of hydrogen on the J-Δa curve during the crack growth stage, the difference between the J value for an effective crack extension of 1 mm ($J_{1.2/BL}$) and the onset of crack growth ($J_{0.2/BL}$) was also determined and denoted as $\Delta J_{0.2\text{-}1.2/BL}$.

The fracture toughness tests of the uncharged specimens were carried out under a nominal displacement rate of 1 mm/min. Nevertheless, based on previous experiences [14,26], hydrogen pre-charged specimens were tested at a displacement rate 100 times lower (0.01 mm/min) to facilitate hydrogen transport towards the highly stressed area near the crack tip, maximizing hydrogen accumulation and thus HE. Two specimens of each grade were tested for both uncharged and hydrogen pre-charged conditions to assure repetitiveness. The mean fracture toughness values and the average standard deviation are provided.

The load and fracture toughness drop caused by the presence of internal hydrogen was assessed by means of the embrittlement index EI, defined in Equation (4), which varies from 0 (no hydrogen embrittlement) to 100% (maximum possible hydrogen embrittlement).

$$EI[\%] = \frac{X - X_H}{X} \cdot 100 \quad (4)$$

where X and X_H are the corresponding property determined without and with internal hydrogen respectively.

2.5 Observation of microstructures and fracture surfaces

In order to identify the operative fracture micromechanisms and relate them to the embrittlement indexes, a thorough fractographic analysis of the fracture surfaces of all the tested CT specimens was performed in a scanning electron microscope (SEM JEOL-JSM5600)

3. RESULTS

3.1 Microstructure, hardness, and tensile properties in uncharged specimens

The microstructure of the four 42CrMo4 grades consisted of tempered martensite, as can be observed in Figure 1 under a magnification of 5000x. A clear difference is noticed between those grades tempered for short times (30 min and 2h) and those tempered for longer times (24h and 7d). The former are characterized by their microstructural acicularity, with elongated and needle-like carbides precipitated along martensitic lath interfaces. On the contrary, when longer tempering treatments are applied, acicular morphology disappears. Indeed, precipitated carbides have more time to break-up, grow, spherodize and distribute more homogeneously in the microstructure, as seen in Figure 2(d). Table 1 and Figure 2 clearly show that as the tempering time increases the hardness and strength parameters (σ_{ys} and σ_{uts}) decrease while ductility parameters (e and RA) increase.

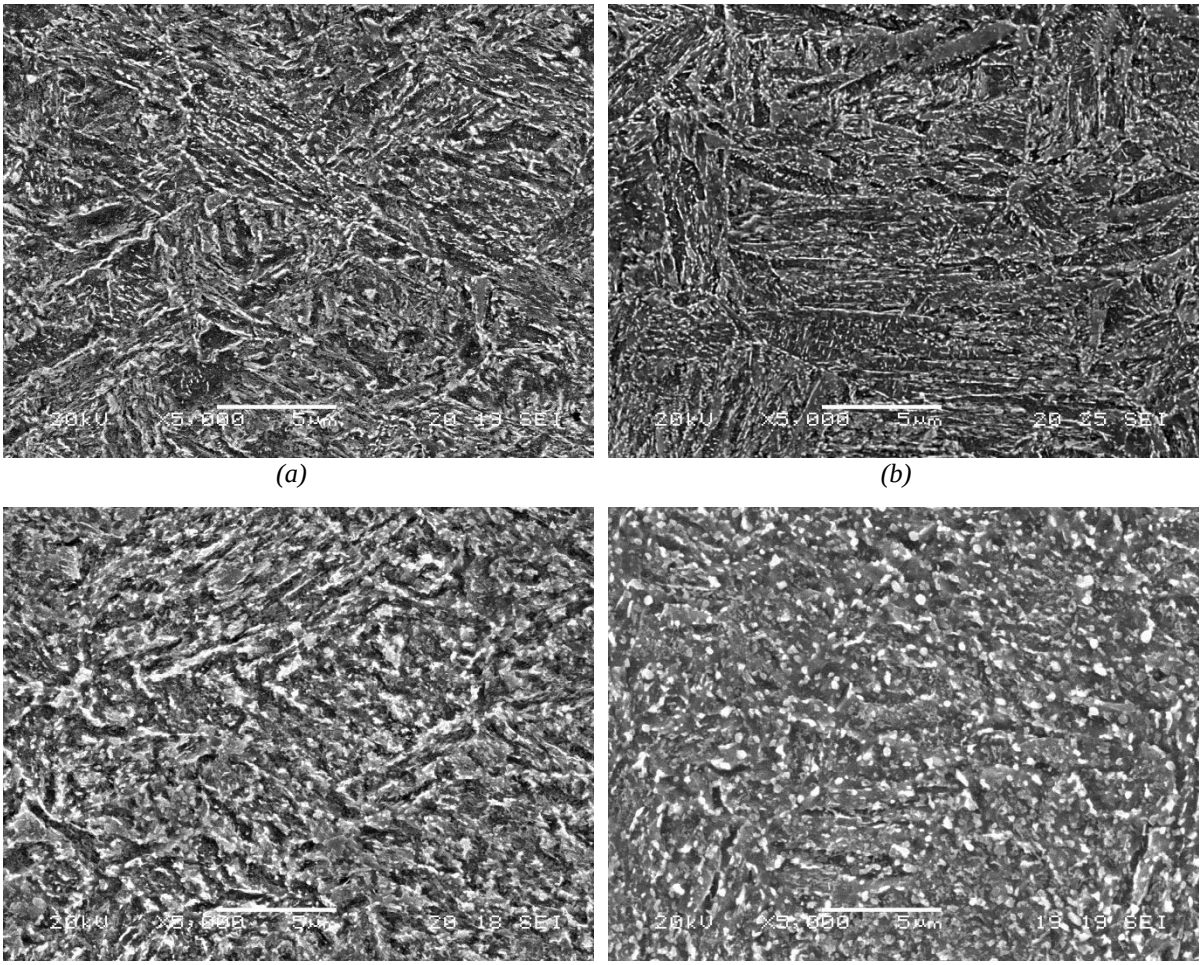

(a) *(b)*

(c) *(d)*

Figure 1. SEM microstructures of 42CrMo4 steel quenched and tempered at 600ºC for (a) 30 min, (b)2h, (c) 24h and (d) 7d.

Based on these microstructural observations and the evolution of the *HV30* hardness and tensile properties presented in Figure 2, it is evident that increasing the duration of tempering promotes microstructural recovery and stress relaxation, as well as a reduction in the density of internal interfaces, where dislocations tend to accumulate [20]. In fact, considering that hardness and strength are indirect indicators of the dislocation density [33], these results also indicate that the dislocation density of these martensitic microstructures decreases when the tempering time is increased.

Grade	Heat treatment	*HV30*	σ_{ys} [MPa]	σ_{uts} [MPa]	*e* [%]	*RA* [%]
QT600-30min	845ºC+WQ+T600ºC/30min	332±3	1020±1	1107±1	12.5±0.7	49.5±0.8
QT600-2h	845ºC+WQ+T600ºC/2h	304±6	880±1	985±2	14.6±0.2	55.4±1.0
QT600-24h	845ºC+WQ+T600ºC/24h	280±7	827±1	920±1	15.8±0.4	51.8±0.6
QT600-7d	845ºC+WQ+T600ºC/7d	247±4	713±1	791±1	19.6±0.7	57.3±1.4

Table 1. Vickers hardness (HV30) and tensile properties of the different 42CrMo4 grades. Uncharged specimens.

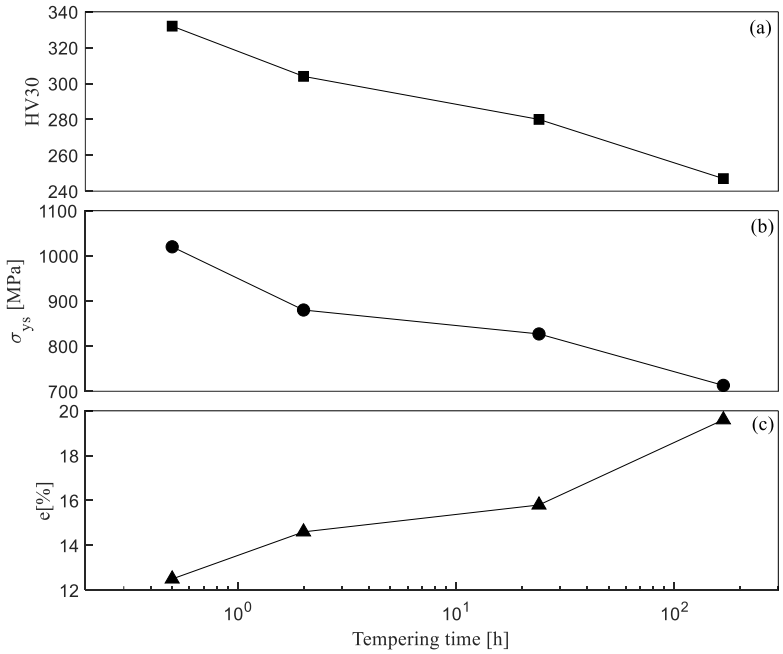

Figure 2. (a) Hardness HV30, (b) yield strength, σ_{ys}, and (c) total elongation, e, plotted against tempering time.

3.2. Diffusivity and trapping capability

The hydrogen desorption curves at room temperature obtained with each steel grade are shown in Figure 3. These figures represent the evolution of hydrogen content, C_H, against the exposure time in air at room temperature, *t*. Notice the very good fitting (R^2>0.97) of the experimental data with exponential functions of the form $C_H = P1 + P2exp(P3 \cdot t)$, which can be used to describe the hydrogen release by diffusion in a cylinder [34,35].

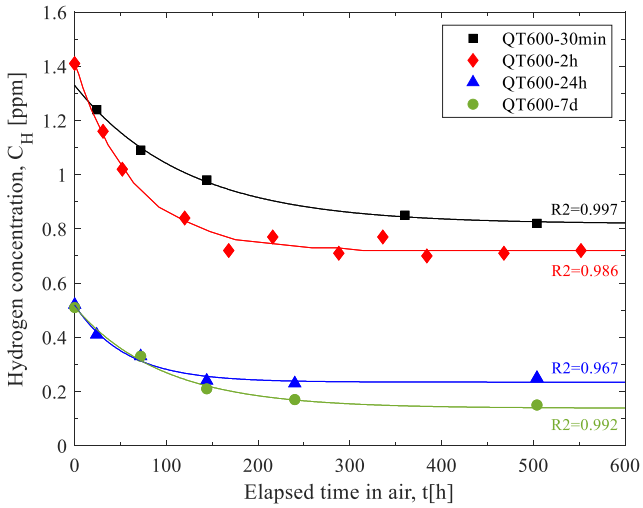

Figure 3. Hydrogen concentration in the microstructure of each steel as a function of the elapsed time in air at room temperature.

The initial hydrogen content, C_{H0}, corresponds to the hydrogen concentration in the steel at time t=0. This parameter represents then the hydrogen concentration at the end of the cooling phase after thermal pre-charging in the hydrogen reactor. On the other hand, the hydrogen concentration measured after a long exposure at room temperature represents the strongly trapped hydrogen concentration, C_{Ht}. This is the hydrogen fraction that is retained in very strong (irreversibly) trapping sites and is not able to egress from the sample at room temperature. The values of these parameters are given in Table 2.

Grade	C_{H0} [wppm]	C_{Ht} [wppm]	D_{app} [m^2/s]
QT600-30min	1.33	0.82	$5.9\pm0.7\times10^{-11}$
QT600-2h	1.41	0.72	$7.4\pm0.5\times10^{-11}$
QT600-24h	0.52	0.25	$1.1\pm0.1\times10^{-10}$
QT600-7d	0.51	0.15	$1.7\pm0.7\times10^{-10}$

Table 2. Initial (C_{H0}) and strongly trapped (C_{Ht}) hydrogen contents obtained from the desorption curves and apparent hydrogen diffusion coefficient (D_{app}) determined in electrochemical permeation tests.

It should be mentioned that despite the hydrogen loses that take place during the cooling phase in the charging reactor, a significant amount of hydrogen still remained in the steels at the moment of testing. It is known that very low hydrogen concentrations (below 0.5 wppm) are enough to provide hydrogen embrittlement in martensitic steels [36]. It is also interesting to note that, as happens with the microstructures, the C_{H0} values are quite similar in those steels tempered for short times (1.3 and 1.4 wppm) and also in those steels tempered for longer times (0.5 wppm). However, C_{Ht} decreases progressively when increasing the tempering time, evidencing a reduction in the density of effective microstructural traps. This is in line with the reduction of dislocation and internal interface densities, as explained in the microstructural analysis (Figure 1) and with the results presented in Figure 2.

Figure 4 shows the normalised permeation curves (J_p/J_{ss} vs. t/L^2) corresponding to the four microstructures, which depend on hydrogen diffusivity and trapping. The dependence of the experimental data on hydrogen content and on sample thickness was removed in this representation dividing the permeation current density, J_p, by the steady-state permeation current density, J_{ss}, reached at the end of the rising transient and the acquisition time, t, by the square of the sample thickness, L.

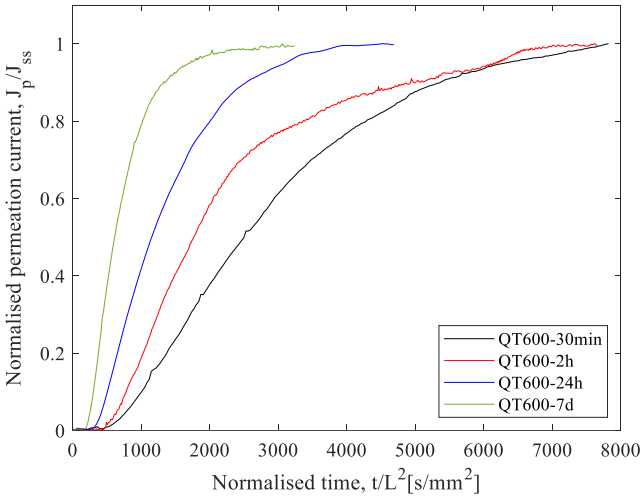

Figure 4. Normalised permeation transients of the four 42CrMo4 grades.

Two main observations can be made about these curves. Firstly, the decrease of the break-through time when the tempering time is increased. This is the time between the beginning of the test (t=0) and the moment at which the

permeation current starts to rise, when the first hydrogen atoms are detected on the other side of the steel membrane. Secondly, the slope of the permeation curve becomes steeper as the tempering time increases. As a result, the time needed to attain the steady-state (J_{ss}), where the permeation flux is practically constant, is lower. In general terms, this behaviour indicates that in less tempered steels, with harder and more distorted microstructures, hydrogen atoms encounter more obstacles during their diffusion through the steel, as the density of hydrogen traps is greater. This is reflected in a decrease of the apparent hydrogen diffusion coefficient when decreasing the tempering time, as reported in Table 2.

3.3 Fracture toughness and micromechanisms

3.3.1. Uncharged specimens

The fracture toughness results of the four grades tested in air without internal hydrogen are shown in Figure 5 and Table 3. Figure 5(a) and (b) display the *P-LLD* curves and the *J-Δa* curves derived from them, respectively. The maximum load reached during the fracture toughness test, P_{max}, the *J* value (average and standard deviation) for the onset of crack growth, $J_{0.2/BL}$, the *J* value for an effective crack growth of 1 mm, $J_{1.2/BL}$, and their difference, $\Delta J_{0.2\text{-}1.2/BL}$, were also determined and are shown in Table 3. The potential law corresponding to the fitted experimental data, $J=C_1\Delta a^{C2}$, is also included.

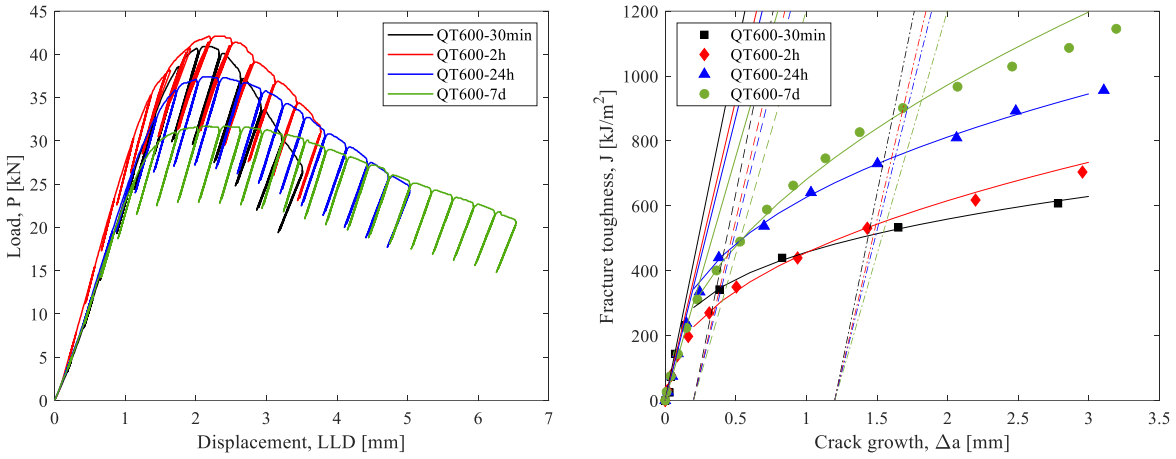

Figure 5. (a) P-LLD and (b) J-Δa curves corresponding to the uncharged specimens (1 mm/min) of the four 42CrMo4 steel grades.

Grade	σ_{ys} [MPa]	P_{max} [kN]	$J_{0.2/BL}$ [kJ/m^2]	$J_{1.2/BL}$ [kJ/m^2]	$\Delta J_{0.2\text{-}1.2/BL}$ [kJ/m^2]	$J=C_1\Delta a^{C2}$	
						C_1	C_2
QT600-30min	1020	40.4±0.7	368±40	530±30	162±10	479±31	0.27±0.03
QT600-2h*	880	42.1	292	545	253	456	0.43
QT600-24h	827	37.1±0.4	474±3	763±15	289±12	632±8	0.38±0.01
QT600-7d	713	32.0±0.5	519±41	941±22	422±19	700±26	0.49±0.03

Table 3. Fracture toughness results of the different 42CrMo4 grades. Uncharged specimens at a displacement rate of 1 mm/min. Only one fracture toughness test was performed in this case*

It is observed that the grades with higher yield strength, tempered for shorter times, reached a higher P_{max} during the fracture tests, and exhibited lower fracture toughness values than those tempered for longer times. The distinction between these two groups is clear when comparing the *J-Δa* curves. This behaviour is in line both with the microstructural observations seen in Figure 1 and with the desorption kinetics reported in Figure 3. It is also interesting to note the flattening of the *J-Δa* curve when the yield strength of the steel increases, as observed also in the progressive reduction of the $\Delta J_{0.2\text{-}1.2/BL}$ parameter.

The only fracture micromechanism identified on the broken surfaces of all the uncharged specimens, regardless the tempering time, was microvoid coalescence (MVC). This ductile mechanism, present along the whole crack extension, is exemplified in Figures 6(a) and (b), for the specimens tempered for 30 min and 7d respectively (highest and lowest yield strengths).

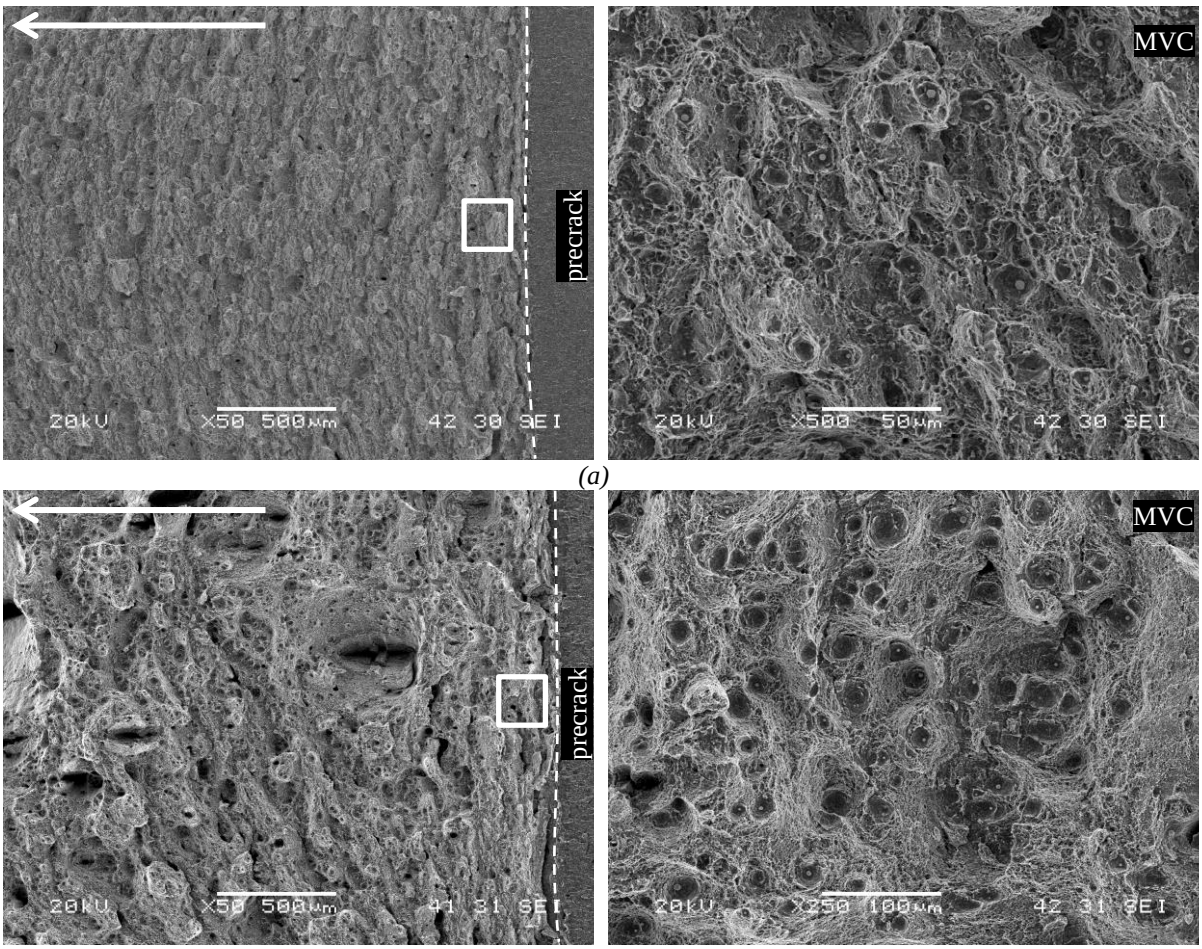

Figure 6. General view of the fracture surfaces (left) and detail of MVC at the onset of crack growth (right) in uncharged CT specimens of (a) QT600-30min and (b) QT600-7d. White arrows indicate the crack growth direction.

3.3.2. Hydrogen pre-charged specimens

The *P-LLD* and *J-Δa* curves obtained with the 42CrMo4 grades tempered for shorter times, in the uncharged (1 mm/min) and H pre-charged (0.01 mm/min) conditions, are shown in Figures 7(a) and (b), respectively. The P_{max} and the fracture toughness values, $J_{0.2/BL}$, $J_{1.2/BL}$ and $\Delta J_{0.2\text{-}1.2/BL}$, along with the test duration, t_{test}, the approximated hydrogen content in the steel's microstructure at the start of the tests (measured on cylindrical pins, Table 2), $C_{H0,}$ and the exponential data fit, are presented in Table 4. Table 5 reports the associated embrittlement indexes.

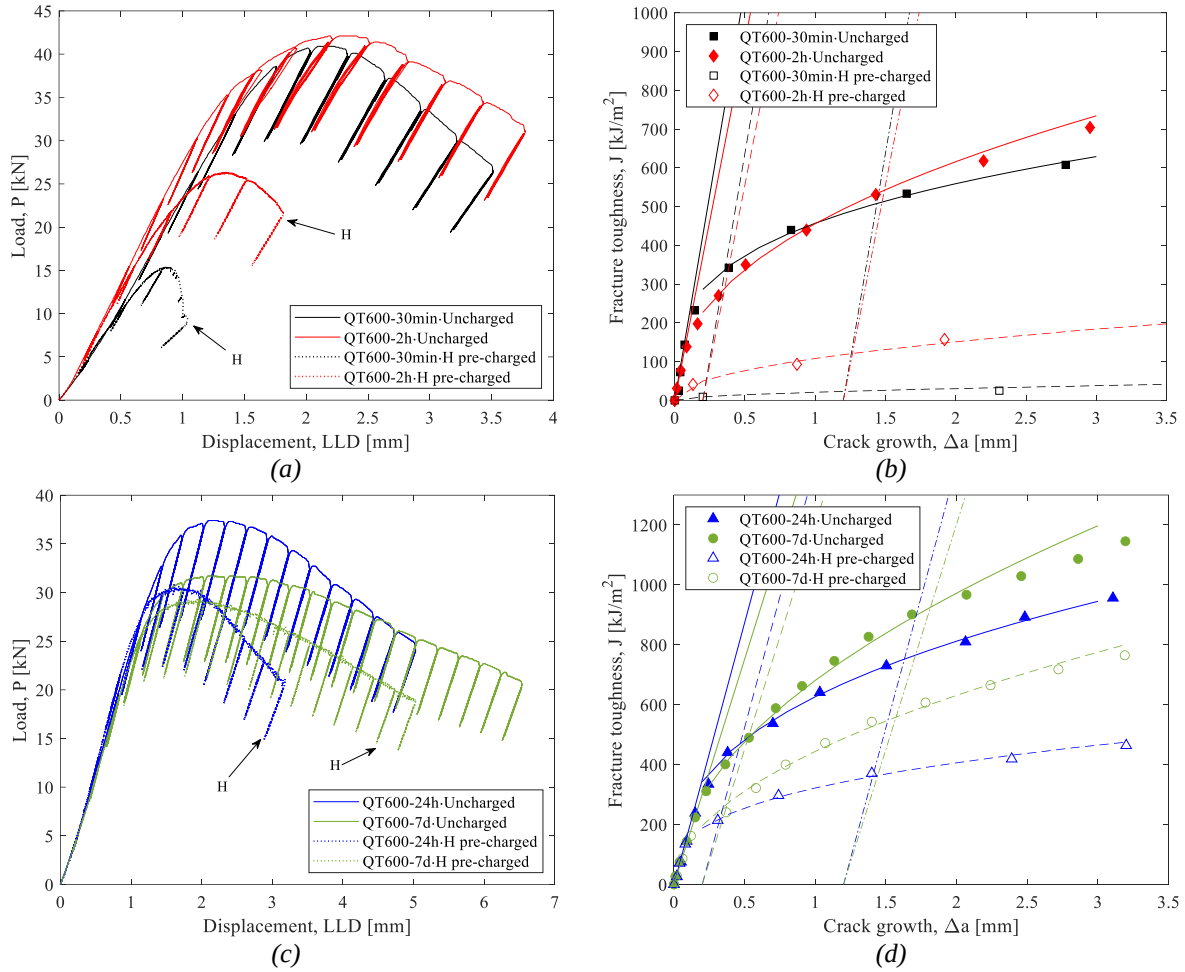

Figure 7. Load-displacement (P-LLD) and fracture toughness-crack growth (J-Δa) curves of uncharged and H pre-charged specimens of (a, b) QT600-30min and QT600-2h and (c, d) QT600-24h and QT600-7d.

Steel	v_{test} [mm/min]	t_{test} [h]	C_{H0} [wppm]	P_{max} [kN]	$J_{0.2/BL}$ [kJ/m²]	$J_{1.2/BL}$ [kJ/m²]	$\Delta J_{0.2\text{-}1.2/BL}$ [kJ/m²]	$J=C_1\Delta a^{C2}$	
								C_1	C_2
QT600-30min	1	0.3	------	40.4±0.7	368±40	530±30	162±10	479±31	0.27±0.03
	0.01	1.4	1.3	15.9±0.8	11±2	25±3	14±1	23±3	0.52±0.04
QT600-2h	1	0.4	------	42.1	292	545	253	456	0.43
	0.01	2.6	1.4	26.8±0.7	66±18	139±28	73±9	120±16	0.42±0.09
QT600-24h	1	0.4	------	37.1±0.4	474±3	763±15	282±12	632±8	0.38±0.01
	0.01	4.9	0.5	31.3±0.7	211±14	349±18	138±4	311±16	0.34±0.01
QT600-7d	1	0.5	------	32.0±0.5	519±41	941±22	422±19	700±26	0.49±0.03
	0.01	8.8	0.5	29.3±0.1	257±17	560±47	303±39	438±48	0.54±0.01

Table 4. Results of the fracture toughness tests performed on uncharged and hydrogen pre-charged CT specimens of 42CrMo4 steel quenched and tempered at 600ºC for different times.

Steel	EI (P_{max}) [%]	EI ($J_{0.2/BL}$) [%]	EI ($J_{1.2/BL}$) [%]	EI ($\Delta J_{0.2\text{-}1.2/BL}$) [%]
QT600-30min	61	97	95	91
QT600-2h	36	77	74	71
QT600-24h	16	56	54	52
QT600-7d	9	51	40	28

Table 5. Average embrittlement indexes relative to P_{max}, $J_{0.2BL}$, $J_{1.2BL}$ and $\Delta J_{0.2\text{-}1.2/BL}$.

Figures 7(a) and (b) illustrate the huge load and fracture toughness drop in the case of the hardest steels when internal hydrogen is present (similar hydrogen contents around 1.4-1.3 wppm). In the grade tempered only for 30 minutes hydrogen embrittlement is maximum, the maximum load and the fracture toughness are reduced more than 60% and 95%, respectively. Indeed, the fast and instable crack growth observed in the *P-LLD* plot as well as the completely flat *J-Δa* curve, with EI($\Delta J_{0.2\text{-}1.2/BL}$) = 91%, are clear signs of the high susceptibility of this steel to HE. Although the fracture properties of hydrogen pre-charged specimens seem to slightly improve when the tempering treatment is extended to 2h (crack growth is more stable now), the fracture toughness reduction is still above 70% along all the crack extension.

The presence of internal hydrogen in the microstructure of these two grades (shorter tempering times) gives rise to considerable alterations of the operative fracture micromechanisms in these mechanical tests, in agreement with the EI values reported in Table 5. As they had similar initial hydrogen concentrations, the operative failure micromechanisms were comparable, as can be observed in Figures 8 and 9. In both cases the fracture micromechanism along the whole crack extension (both at initiation and at propagation stages), was a combination of decohesion along martensitic lath interfaces (MLD), and intergranular fracture (IG). MLD is described in detail in [37].

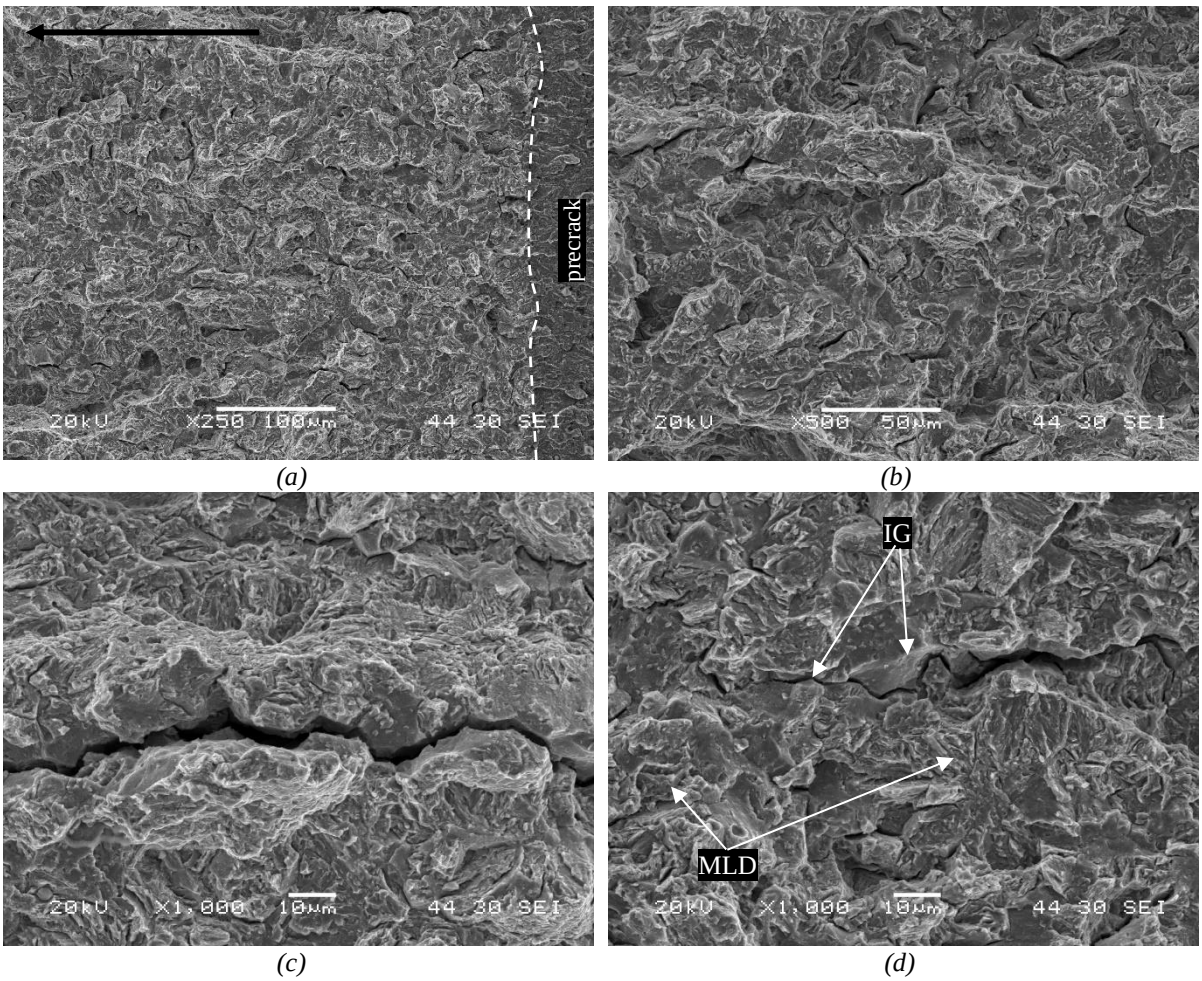

(a) *(b)*

(c) *(d)*

Figure 8. Fracture micromechanisms (SEM) observed in H pre-charged specimens (0.01 mm/min) of QT600-30min steel grade. (a)(b) General view and detail in (c) crack initiation and (d) propagation stages. Black arrow indicate crack growth direction.

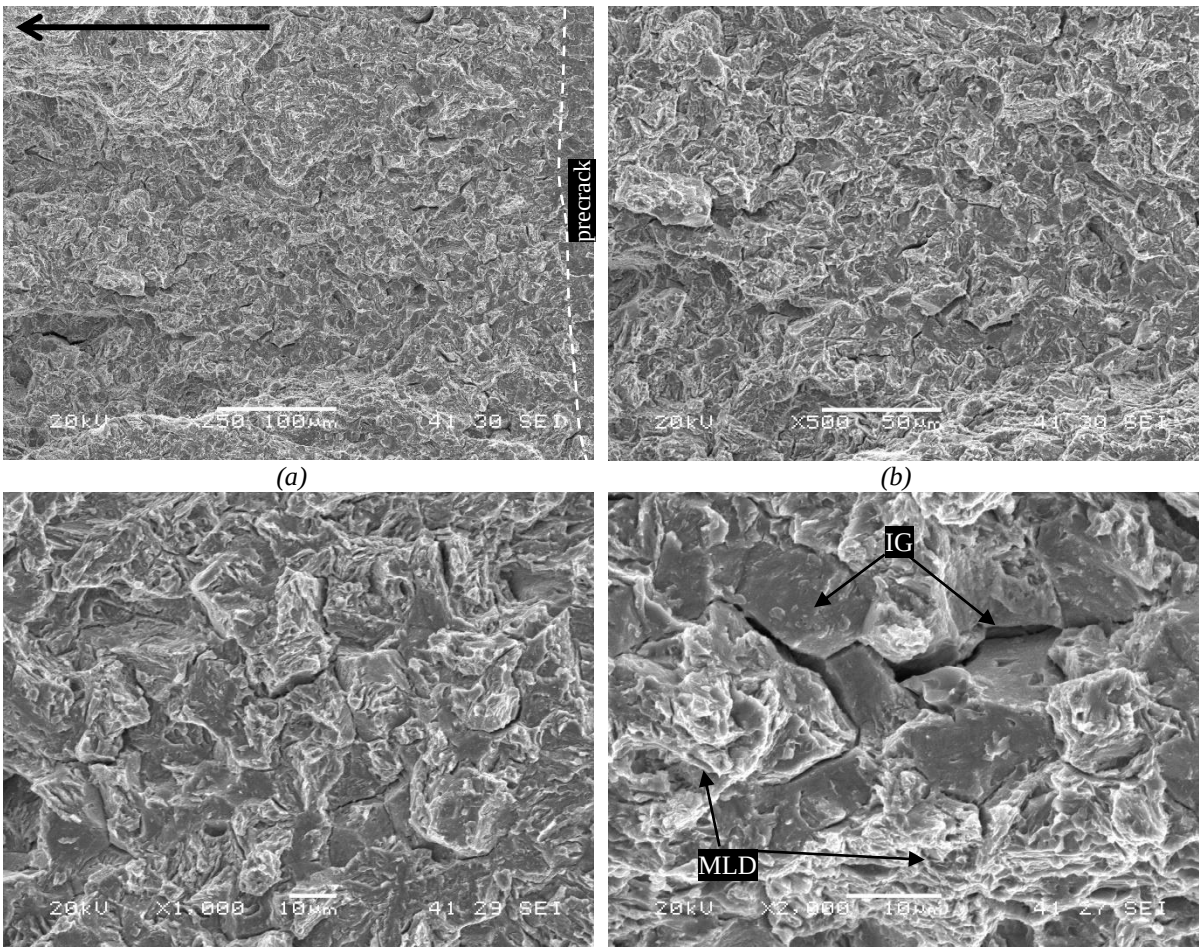

Figure 9. Fracture micromechanisms (SEM) observed in H pre-charged specimens (0.01 mm/min) of QT600-2h steel grade. (a)(b) General view, (c)(d) details at crack initiation. Black arrow indicates crack growth direction.

Figures 7(c) and (d) show the *P-LLD* and *J-Δa* curves of uncharged and H pre-charged specimens tempered for 24h and 7d. Both specimens had an initial hydrogen content of 0.5 wppm. Their associated fracture parameters and embrittlement indexes are included in Tables 4 and 5. When compared to Figures 7(a) and (b), it is clear that the fracture toughness behaviour improved in terms of hydrogen embrittlement with longer tempering treatments. Nevertheless, there is a slight decrease of the maximum load and a significant reduction in fracture toughness due to the presence of internal hydrogen in these grades. In fact, even after 24h of tempering all the fracture related embrittlement indexes remain above 50% (Table 5). On the other hand, the steel tempered for the longest time displayed the lowest sensitivity to HE, with a maximum load drop below 10%. Although the EI reported for the fracture toughness at the onset of crack growth was also around 50% in this grade, after 1 mm of crack growth it dropped to 40%, leading to a decrease of less than 30% of the $\Delta J_{0.2\text{-}1.2/BL}$ parameter. Thus, the steel tempered for 7 days had the greatest resistance to crack propagation in presence of hydrogen.

The fracture surfaces of the specimens tested under internal hydrogen in the QT600-24h steel are shown in Figure 10. The general view of Figure 10(a) reveals the presence of an initial region, with an extension of around 500-900 µm, characterized by a softer topography. A detailed view of this area, shown in Figures 10(b) and (c), shows the presence of MLD as well as secondary cracking. After this initial zone, the predominant micromechanism is MVC, as in the uncharged specimen. However, some brittle spots characterized by MLD, such as the one shown in Figure 10(d), are still noticed.

In the same way, a general view of the fracture surface of the hydrogen pre-charged QT600-7d steel, Figure 11(a) and (b), also reveals the existence of an initial region where hydrogen has fostered MLD micromechanism. In this case its extension was limited to 275-300 µm from the precrack. A detail of this area is shown in Figure 11(c). On

the other hand, the main failure micromechanism operative in the crack propagation region is MVC, with very occasional MLD regions like the one shown in Figure 11(d).

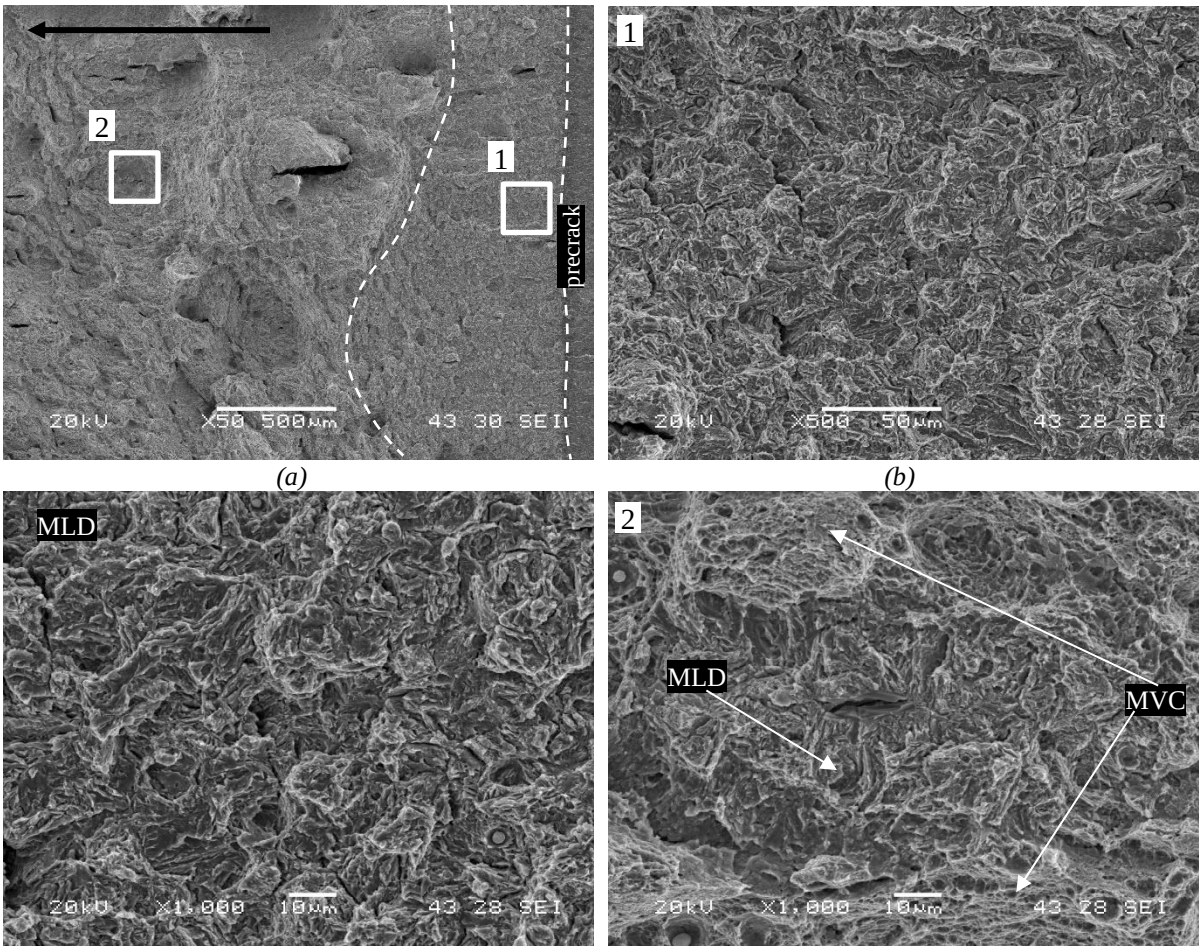

Figure 10. Fracture micromechanisms observed in H pre-charged specimens (0.01 mm/min) of QT600-24h steel. (a) General view, (b)(c) detail at the crack initiation region and (d) detail at the crack propagation region. Black arrow indicates crack growth direction.

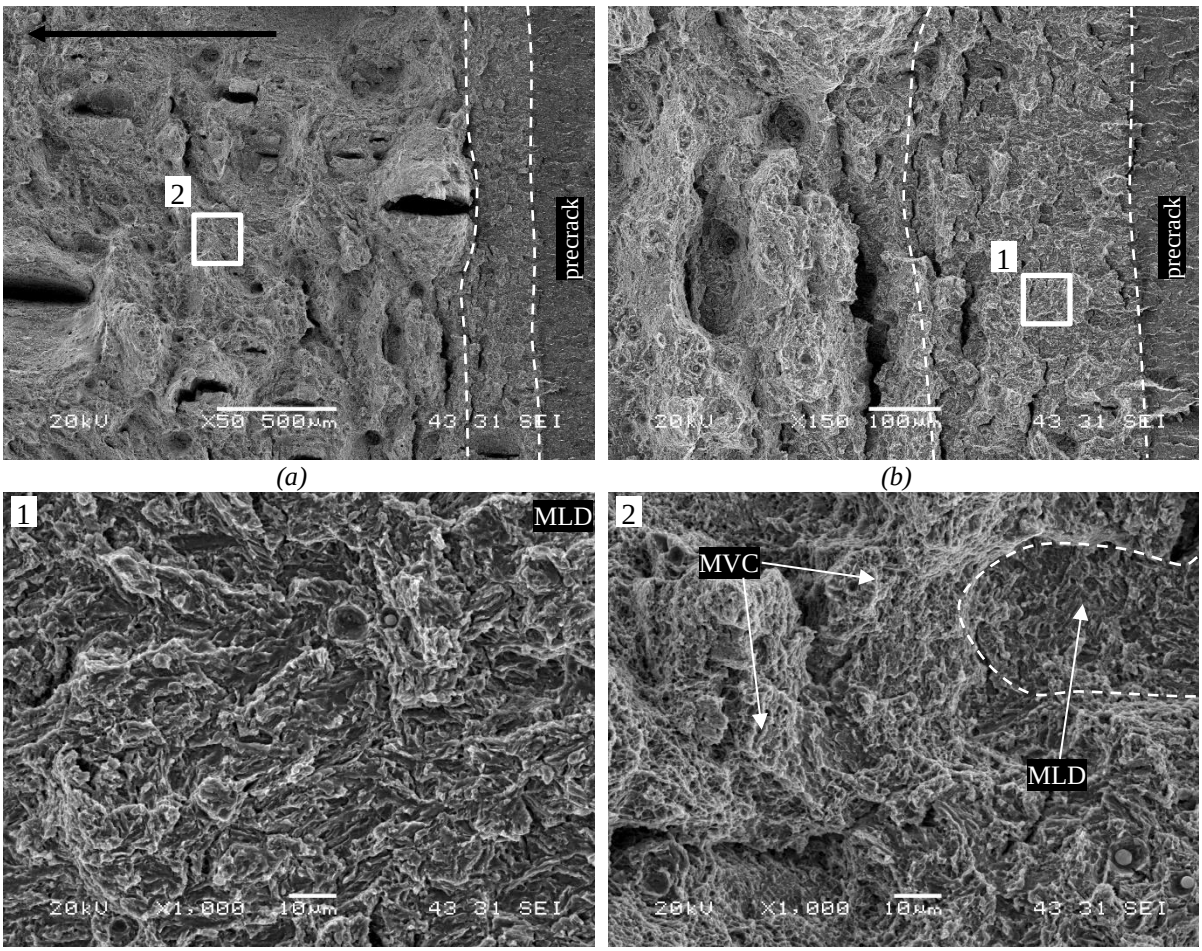

(a) *(b)*

(c) *(d)*

Figure 11. Fracture micromechanisms observed in H pre-charged specimens (0.01 mm/min) of QT600-7d steel. (a)(b) General views, (c) detail of the crack initiation region and (d) detail of the crack propagation region. Black arrow indicates crack growth direction.

4. DISCUSSION

HE is governed by the complex interplay of a local stress state and a local hydrogen concentration in the process region just ahead of the crack tip [38–40]. Therefore, the yield strength as well as the density of hydrogen traps, N_t, are good indicators of the susceptibility of the steel to this phenomenon.

Figure 12(a) depicts the relationship between the duration of the tempering treatment (in logarithmic scale), the apparent diffusion coefficients, D_{app}, and the strongly trapped hydrogen, C_{Ht}, of the four studied grades. D_{app} increases and C_{Ht} decreases with the duration of the tempering treatment. Considering these trends, together with the microstructural interpretation explained above, it can be said that increasing the tempering time gives rise to a more recovered and less distorted microstructure, with less capacity to retain hydrogen and therefore less obstacles that hinder hydrogen diffusion.

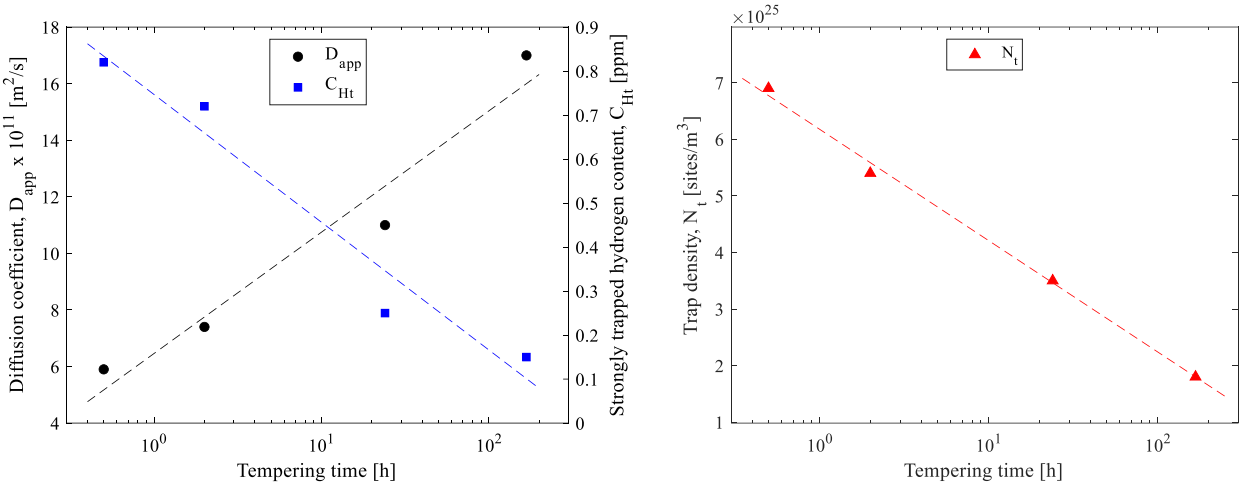

Figure 12. Evolution of the (a) apparent diffusion coefficient, D_{app}, and strongly trapped hydrogen, C_{Ht}, and (b) density of trapping sites, N_t, with the tempering time.

Indeed, Equation 5 is frequently employed to correlate the density of hydrogen trapping sites, N_t, with D_{app} when trap occupancy is low [41].

$$N_t = N_L \left(\frac{D_L}{D_{app}} - 1 \right) \cdot exp\left(-\frac{E_b}{R \cdot T} \right) \quad (5)$$

where N_L represents the density of interstitial lattice sites, D_L the lattice diffusion coefficient, E_b the trap binding energy, R the gas constant and T the temperature. These parameters can be assumed to be practically constant in the studied 42CrMo4 grades, being possible to estimate the density of trapping sites. For tetrahedral interstitial sites in the BCC Fe crystal lattice N_L has a value of 5.1×10^{29} sites/m^3 [42]. D_L has been reported to be in the order of 7.3×10^{-9} m^2/s [43] for undeformed pure iron, however in a distorted martensitic lattice this value is usually lower [44,45]. Zafra et al. [46] reported D_L values between 3.8 and 7.6×10^{-10} m^2/s for a 42CrMo4 steel quenched and tempered between 500 and 700ºC, so an average value of 5.7×10^{-10} m^2/s was considered in this work. These same authors [46] also demonstrated that the tempering temperature has no relevant influence on the nature of the existing traps, and determined an average E_b of 27.4 kJ/mol for hydrogen trapped in dislocations. The same trapping response is expected when the tempering time is modified keeping the tempering temperature constant. Consequently, being widely accepted that dislocations, which are frequently piled-up in internal interfaces, constitute the governing hydrogen trap in martensitic microstructures of CrMo steels [47,48], a E_b =27.4 kJ/mol was used to estimate N_t.

The N_t values obtained for each studied grade by means of Equation (5), considering the D_{app} determined through hydrogen permeation tests (Table 3), are reported in Table 6. These values are comparable to those obtained by other authors in similar CrMo steels [44,49,50]. For example, Si et al. [50] obtained a trap density of 3.7×10^{25}

sites/m^3 in a 1Cr0.12Mo0.2Ni steel quenched and tempered at 600ºC for 3h. Figure 12(b) shows the evolution of N_t with the tempering time. In line with the evolution of D_{app} and C_{Ht}, longer tempering times lead to a considerable reduction of the number of microstructural hydrogen traps in the steel (mainly dislocations).

Grade	N_t [sites/m^3]
QT600-30min	6.9×10^{25}
QT600-2h	5.4×10^{25}
QT600-24h	3.5×10^{25}
QT600-7d	1.8×10^{25}

Table 6. Density of trapping sites, N_t, estimated in all the studied grades.

It is then clear that the N_t parameter constitute a useful indicator of the dislocation density in martensitic CrMo steels. This fact is of great relevance, as dislocations play an essential role in hydrogen trapping and in embrittlement mechanisms. Once the presence of hydrogen atoms reduce the Peierls stress in the steel, facilitating the movement of dislocations (HELP) [8], dislocations themselves are also able to transport hydrogen atoms to the highly stressed and strained region developed ahead of the crack tip. Therefore, under the same internal hydrogen concentration, hydrogen accumulation into the crack tip process zone increases significantly in steels with greater N_t (dislocation density).

Figure 13 also shows that increasing the yield strength of the steel, increases the density of hydrogen trapping sites. This means that during the fracture test the magnitude of the hydrostatic stress, σ_H, ($2.5\sigma_{ys}$) [51] developed in the crack front region is greater. Therefore, more hydrogen atoms will move towards this region (Equation 1), where they accumulate in internal interfaces. Eventually, when the local hydrogen concentration in this zone, C_{Hloc}, reaches a critical hydrogen concentration, C_{Hcrit}, decohesion between these internal interfaces can take place under abnormally low stress values. Failure will occur then due to the HEDE mechanism, that is manifested as MLD and/or IG features in fracture surfaces (see Figures from 8 to 11). The process through which HE takes place in a hydrogen pre-charged CT specimen is represented schematically in Figure 14 for two steels with different yield strength ($\sigma_{ys1}>\sigma_{ys2}$). In addition, the use of low displacement rates is significant in this embrittling process as hydrogen is transported towards the process zone for longer times leading to higher hydrogen accumulation in the process zone [52]. In other words, a higher yield strength not only implies that in a stress-free situation the density of trapping sites in the steel is higher, but also that hydrogen accumulation in the process zone will be multiplied during mechanical loading.

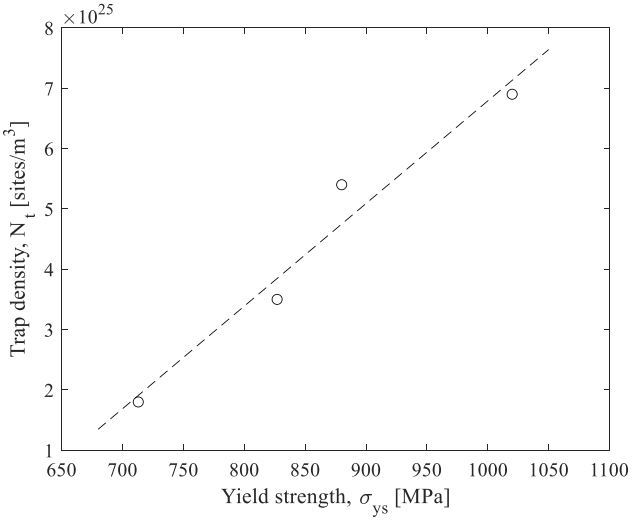

Figure 13. Relationship between the yield strength, σ_{ys}, and the trap density, N_t.

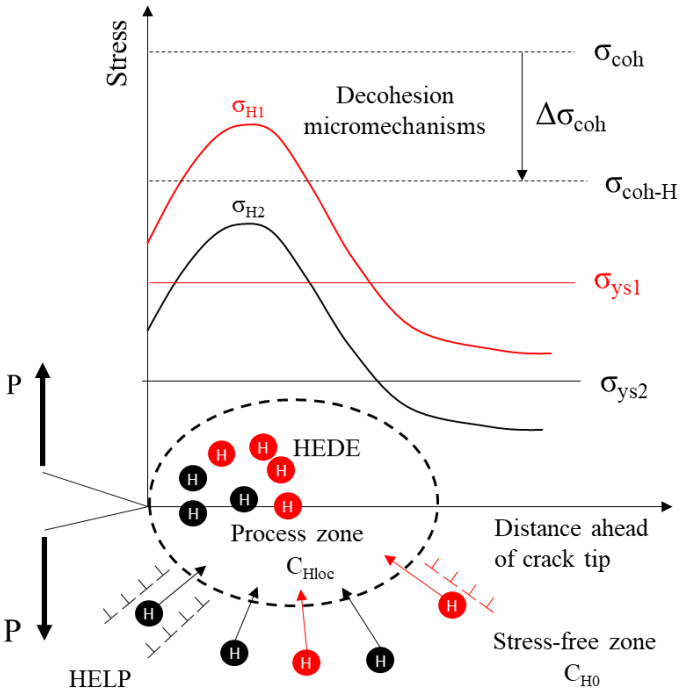

Figure 14. Cohesive strength reduction ($\Delta\sigma_{coh}$) of grain boundaries and lath interfaces due to hydrogen. σ_{coh} represents the cohesive strength of the uncharged steel and $\sigma_{coh\text{-}H}$ represents the cohesive strength of the steel with internal hydrogen.

The influence of yield strength on HE sensitivity is illustrated in Figure 15, which shows the evolution of the $J_{0.2/BL}$ embrittlement index in terms of the yield strength of the steel. It is observed that EI($J_{0.2/BL}$) increases linearly with σ_{ys}, with a good correlation coefficient (R^2=0.912). The predominant fracture micromechanisms (and their extension in the fracture surface), as well as C_{H0} are indicated in this figure.

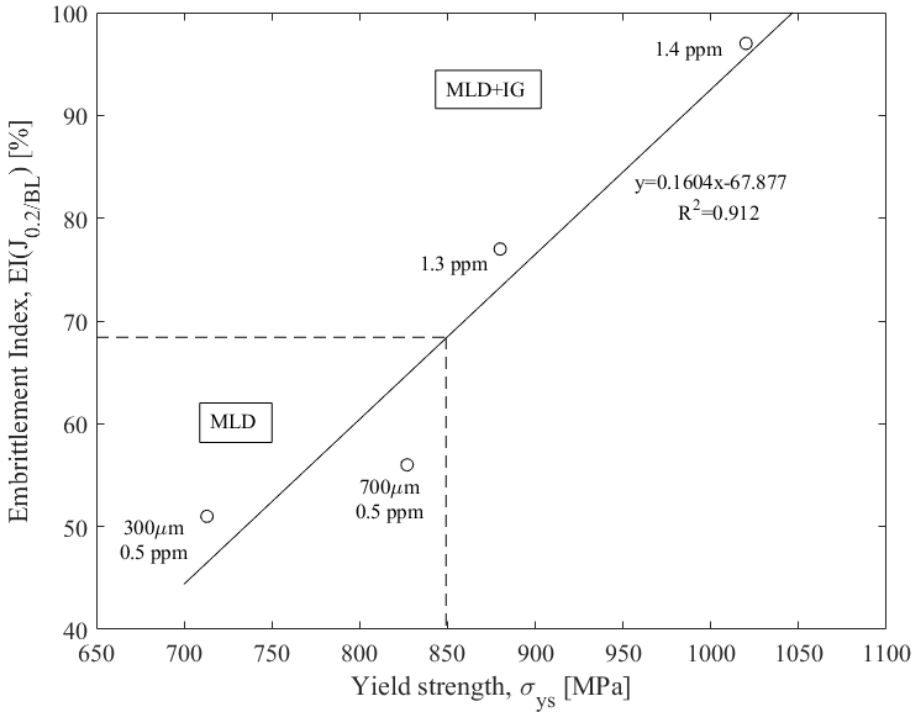

Figure 15. Embrittlement index relative to $J_{0.2/BL}$ parameter, EI($J_{0.2/BL}$), as a function of the steel yield strength, σ_{ys}. Operative fracture micromechanisms showing their extension and approximate hydrogen contents.

Brittle hydrogen micromechanisms (MLD+IG) were present throughout the whole fracture surface in the two steels with the highest yield strengths. However, in the case of the two steels with the lowest yield strengths, a C_{H0} of 0.5 wppm is not high enough to reach the critical concentration in the crack tip which would trigger grain boundary decohesion. MLD is therefore the operative mechanism for crack growth initiation of the grades tempered for longer times. Nevertheless, even under the same C_{H0}, the higher σ_{ys} and N_t of the steel tempered for 24h gives rise to a slight increase in the embrittlement index and the initial region affected by MLD increases from 300 to 700 μm. When the yield strength of the steel is further increased as a result of applying a shorter tempering treatment, the embrittlement index drastically increases and IG micromechanism is present along the whole fracture surface extension. As happened before, despite both high strength grades having similar C_{H0} values (1.3-1.4 wppm), the steel with the higher σ_{ys} (higher σ_H in the process zone) had a maximum $J_{0.2/BL}$ reduction, above 95%.

It is clear than under a tempering temperature of 600ºC, even the long treatments applied in this work, 24h and 7d, are insufficient to minimize HE, as fracture toughness reductions of about 50% are still unacceptable for a safe structural design, implying the use of large safety factors with the resulting increase of costs. Considering the linear trend proposed in Figure 15, to reduce HE to an admissible value, for example EI($J_{0.2/BL}$) below 15%, a steel with a yield strength lower than 515 MPa should be used for the manufacturing of hydrogen pressure vessels. However, assuming a linear trend in Figure 2(b) for the yield strength vs. the tempering time, a tempering treatment of nearly 500 days at 600ºC would be necessary, which is obviously impractical and excessively costly.

The $J_{0.2/BL}$ fracture toughness results and corresponding hydrogen embrittlement indexes, EI, in presence of hydrogen were represented in Figure 15 against the Hollomon-Jaffe tempering parameter, including also previous results [26] obtained with the same steel quenched and tempered at 600, 650 and 700ºC for 2 hours. Although more tests are needed, tempering parameter seems to offer a certain confidence to extrapolate fracture toughness hydrogen embrittlement results. According to Equation 2, the Hollomon-Jaffe tempering parameter, P, corresponding to that tempering treatment (600ºC for 470 days) is 14432. Therefore, an equivalent treatment - with the same P - could be easily attained by applying a tempering treatment at 700ºC for 4h. Nevertheless, it is obvious then that more research is needed on thermal treatments in order to find the 42CrMo4 grade most suitable for high hydrogen pressure applications.

5. CONCLUSIONS

The effects of internal hydrogen on the fracture toughness of a 42CrMo4 steel quenched and tempered at 600ºC for different times (30 min, 2 h, 24 h and 7 d) was researched in this work. The hydrogen diffusivity and trapping capability of the studied microstructures were assessed by means of electrochemical permeation tests and the determination of hydrogen desorption curves. Finally, a thorough fractographic analysis was performed in order to identify the prevalent hydrogen embrittlement mechanisms. The following conclusions were obtained:

- As tempering time was increased from 30 min to 7 days, the distortion and acicularity of the martensitic microstructure was reduced, as well as its dislocation density. These facts explain the reduction in hardness and strength of the steel with the increase of tempering duration.
- The desorption kinetics of those grades submitted to shorter treatments, 30 min and 2h, were very similar. The same occurs with the steel grades tempered for longer times, 24h and 7d. In both groups, the initial hydrogen content measured using TDA was comparable, 1.3-1.4 and 0.5 wppm respectively. Nevertheless, D_{app} increases and C_{Ht} decreases with longer tempering times. This is due to a reduction of the dislocation density and therefore the density of hydrogen traps.
- The fracture toughness of all the studied grades was considerably reduced by the presence of internal hydrogen, and the fracture micromechanisms were also affected. Indeed, as the yield strength of the steel increased (shorter tempering treatments), the embrittlement index associated to the $J_{0.2/BL}$ parameter increased linearly, attaining values as high as 95%.
- Whereas microvoid coalescence was the operative micromechanism in all the uncharged steel grades, the fracture toughness drop reported in the hydrogenated specimens is explained by a change in the failure

micromechanisms: decohesion along martensitic lath interfaces (MLD) and even intergranular fracture (IG) in the strongest, less tempered grades.

- Finally, due to the high embrittlement indexes for the onset of crack growth ($J_{0.2/BL}$) reported in all the grades - always higher than 50% -, the studied heat treatments are not recommended for applications where cracks may grow in the presence of hydrogen. Alternative heat treatments, such as high temperature tempering treatments should be investigated in order to provide a suitable 42CrMo4 grade for the manufacturing of welded pipes and pressure vessels containing high-pressure hydrogen gas.

ACKNOWLEDGEMENTS

The authors would like to thank the Spanish Ministry of Science, Innovation and Universities for the financial support received to carry out research project RTI2018-096070-B-C31 (H2steelweld). Likewise, the SIMUMECAMAT research group appreciates the help of the Principality of Asturias through the Science, Technology and Innovation Plan (IDI/2018/0000134). A. Zafra and G. Álvarez thank the regional government of the Principality of Asturias for the Severo Ochoa grants PA-18-PF-BP17-038 and PA-20-PF-BP19-087, respectively. Finally, the authors would also like to acknowledge the technical support provided by the Scientific and Technical Service of the University of Oviedo for the use of the SEM JEOLJSM5600 scanning electron microscope.

REFERENCES

[1] M. Dadfarnia, P. Sofronis, T. Neeraj, Hydrogen interaction with multiple traps: Can it be used to mitigate embrittlement?, Int. J. Hydrogen Energy. 36 (2011) 10141–10148. https://doi.org/10.1016/j.ijhydene.2011.05.027.

[2] R.A. Oriani, The diffusion and trapping of hydrogen in steel, Acta Metall. 18 (1970) 147–157. https://doi.org/10.1016/0001-6160(70)90078-7.

[3] Y. Wang, X. Wu, Z. Zhou, X. Li, Numerical analysis of hydrogen transport into a steel after shot peening, Results Phys. 11 (2018) 5–16. https://doi.org/10.1016/j.rinp.2018.08.030.

[4] A. McNabb & P.K. Foster, A new analysis of the diffusion of hydrogen in iron and ferritic steels, Trans. Met. Soc. AIME. 227 (1963) 618–27.

[5] J.Y. Lee, J.L. Lee, A trapping theory of hydrogen in pure iron, Philos. Mag. A Phys. Condens. Matter, Struct. Defects Mech. Prop. 56 (1987) 293–309. https://doi.org/10.1080/01418618708214387.

[6] I.M. Robertson, P. Sofronis, A. Nagao, M.L. Martin, S. Wang, D.W. Gross, K.E. Nygren, Hydrogen Embrittlement Understood, Metall. Mater. Trans. B Process Metall. Mater. Process. Sci. 46 (2015) 1085–1103. https://doi.org/10.1007/s11663-015-0325-y.

[7] T. Michler, C. San Marchi, J. Naumann, S. Weber, M. Martin, Hydrogen environment embrittlement of stable austenitic steels, Int. J. Hydrogen Energy. 37 (2012) 16231–16246. https://doi.org/10.1016/j.ijhydene.2012.08.071.

[8] S.P. Lynch, Hydrogen embrittlement (HE) phenomena and mechanisms, Stress Corros. Crack. Theory Pract. (2011) 90–130. https://doi.org/10.1533/9780857093769.1.90.

[9] Z.D. Harris, S.K. Lawrence, D.L. Medlin, G. Guetard, J.T. Burns, B.P. Somerday, Elucidating the contribution of mobile hydrogen-deformation interactions to hydrogen-induced intergranular cracking in polycrystalline nickel, Acta Mater. 158 (2018) 180–192. https://doi.org/10.1016/j.actamat.2018.07.043.

[10] M. Nagumo, Hydrogen related failure of steels - A new aspect, Mater. Sci. Technol. 20 (2004) 940–950. https://doi.org/10.1179/026708304225019687.

[11] R. Srinivasan, T. Neeraj, Hydrogen embrittlement of ferritic steels: Deformation and failure mechanisms and challenges in the oil and gas industry, Jom. 66 (2014) 1377–1382. https://doi.org/10.1007/s11837-014-1054-4.

[12] A. Barnoush, H. Vehoff, Recent developments in the study of hydrogen embrittlement: Hydrogen effect on dislocation nucleation, Acta Mater. 58 (2010) 5274–5285. https://doi.org/10.1016/j.actamat.2010.05.057.

[13] M.B. Djukic, G.M. Bakic, V. Sijacki Zeravcic, A. Sedmak, B. Rajicic, The synergistic action and interplay of hydrogen embrittlement mechanisms in steels and iron: Localized plasticity and decohesion, Eng. Fract. Mech. 216 (2019) 106528. https://doi.org/10.1016/j.engfracmech.2019.106528.

[14] A. Zafra, G. Alvarez, J. Belzunce, J.M. Alegre, C. Rodríguez, Fracture toughness of coarse-grain heat affected zone of quenched and tempered CrMo steels with internal hydrogen: fracture micromechanisms, Eng. Fract. Mech. 241 (2021) 107433.

[15] A. Nagao, C.D. Smith, M. Dadfarnia, P. Sofronis, I.M. Robertson, Interpretation of Hydrogen-induced Fracture Surface Morphologies for Lath Martensitic Steel, Procedia Mater. Sci. 3 (2014) 1700–1705. https://doi.org/10.1016/j.mspro.2014.06.274.

[16] E. Ohaeri, U. Eduok, J. Szpunar, Hydrogen related degradation in pipeline steel: A review, Int. J. Hydrogen Energy. 43 (2018) 14584–14617. https://doi.org/10.1016/j.ijhydene.2018.06.064.

[17] R. Miresmaeili, L. Liu, H. Kanayama, A possible explanation for the contradictory results of hydrogen effects on macroscopic deformation, Int. J. Press. Vessel. Pip. 99–100 (2012) 34–43. https://doi.org/10.1016/j.ijpvp.2012.08.001.

[18] X. Li, B. Gong, C. Deng, Y. Li, Effect of pre-strain on microstructure and hydrogen embrittlement of K-TIG welded austenitic stainless steel, Corros. Sci. 149 (2019) 1–17. https://doi.org/10.1016/j.corsci.2018.12.018.

[19] C. Colombo, A. Zafra García, J. Belzunce, I. Fernandez Pariente, Sensitivity to hydrogen embrittlement of AISI 4140 steel: A numerical study on fracture toughness, Theor. Appl. Fract. Mech. 110 (2020). https://doi.org/10.1016/j.tafmec.2020.102810.

[20] G. Krauss, Martensite in steel: Strength and structure, Mater. Sci. Eng. A. 273–275 (1999) 40–57. https://doi.org/10.1016/s0921-5093(99)00288-9.

[21] EIGA, Hydrogen cylinders and transport vessels, Doc 100/20, European Industrial Gases Association, Brussels, 2020.

[22] D.R.G. Mitchell, C.J. Moss, R.R. Griffiths, Optimisation of post-weld heat treatment of a 1.25Cr-0.5Mo pressure vessel for high temperature hydrogen service, Int. J. Press. Vessel. Pip. 76 (1999) 259–266. https://doi.org/10.1016/S0308-0161(98)00131-8.

[23] T. Dai, J.C. Lippold, The effect of postweld heat treatment on hydrogen-assisted cracking of f22/625 overlays, Weld. J. 97 (2018) 75S-90S. https://doi.org/10.29391/2018.97.007.

[24] Y. Song, M. Chai, W. Wu, Y. Liu, M. Qin, G. Cheng, Experimental investigation of the effect of hydrogen on fracture toughness of 2.25Cr-1Mo-0.25V steel and welds after annealing, Materials (Basel). 11 (2018) 1–14. https://doi.org/10.3390/ma11040499.

[25] M. Tvrdý, S. Havel, L. Hyspecká and K. Mazanec, Hydrogen embrittlement of CrMo and CrMoV pressure vessel steels, Int. J. Pres. Ves. Pip. 9 (1981) 355–365.

[26] A. Zafra, L.B. Peral, J. Belzunce, C. Rodríguez, Effects of hydrogen on the fracture toughness of 42CrMo4 steel quenched and tempered at different temperatures, Int. J. Press. Vessel. Pip.

171 (2019) 34–50. https://doi.org/10.1016/j.ijpvp.2019.01.020.

[27] A. Zafra, L.B. Peral, J. Belzunce, C. Rodríguez, Effect of hydrogen on the tensile properties of 42CrMo4 steel quenched and tempered at different temperatures, Int. J. Hydrogen Energy. 43 (2018) 9068–9082. https://doi.org/10.1016/j.ijhydene.2018.03.158.

[28] A. Díaz, A. Zafra, E. Martínez-Pañeda, J.M. Alegre, J. Belzunce, I.I. Cuesta, Simulation of hydrogen permeation through pure iron for trapping and surface phenomena characterisation, Theor. Appl. Fract. Mech. 110 (2020). https://doi.org/10.1016/j.tafmec.2020.102818.

[29] ASTM G148, Standard practice for evaluation of hydrogen uptake, permeation, and transport in metals by an electrochemical technique, ASTM Int. (2011).

[30] F.D. Fischer, G. Mori, J. Svoboda, Modelling the influence of trapping on hydrogen permeation in metals, Corros. Sci. 76 (2013) 382–389. https://doi.org/10.1016/j.corsci.2013.07.010.

[31] A. Zafra, J. Belzunce, C. Rodríguez, Hydrogen diffusion and trapping in 42CrMo4 quenched and tempered steel: influence of quenching temperature and plastic deformation, Mater. Chem. Phys. 255 (2020) 123599.

[32] F.M. Testing, ASME E1820-01Standard Test Method for Measurement of Fracture Toughness, (2001). https://doi.org/10.1520/E1820-09.2.

[33] S. Takebayashl, T. Kunieda, N. Yoshinaga, K. Ushioda, S. Ogata, Comparison of the dislocation density in martensitic steels evaluated by some X-ray diffraction methods, ISIJ Int. 50 (2010) 875–882. https://doi.org/10.2355/isijinternational.50.875.

[34] J. Crank, The Mathematics of Diffusion, 2nd Ed. Oxford Univ. Press. UK. (1975). https://doi.org/10.1016/0306-4549(77)90072-X.

[35] C.J.C. Filho, M.B. Mansur, P.J. Modenesi, B.M. Gonzalez, The effect of hydrogen release at room temperature on the ductility of steel wire rods for pre-stressed concrete, Mater. Sci. Eng. A. 527 (2010) 4947–4952. https://doi.org/10.1016/j.msea.2010.04.042.

[36] A. Trautmann, G. Mori, M. Oberndorfer, S. Bauer, C. Holzer, C. Dittmann, Hydrogen uptake and embrittlement of carbon steels in various environments, Materials (Basel). 13 (2020). https://doi.org/10.3390/MA13163604.

[37] A. Nagao, M. Dadfarnia, B.P. Somerday, P. Sofronis, R.O. Ritchie, Hydrogen-enhanced-plasticity mediated decohesion for hydrogen-induced intergranular and "quasi-cleavage" fracture of lath martensitic steels, J. Mech. Phys. Solids. 112 (2018) 403–430. https://doi.org/10.1016/j.jmps.2017.12.016.

[38] P. Sofronis, R.M. McMeeking, Numerical analysis of hydrogen transport near a blunting crack tip, J. Mech. Phys. Solids. 37 (1989) 317–350. https://doi.org/10.1016/0022-5096(89)90002-1.

[39] E.I. Galindo-Nava, B.I.Y. Basha, P.E.J. Rivera-Díaz-del-Castillo, Hydrogen transport in metals: Integration of permeation, thermal desorption and degassing, J. Mater. Sci. Technol. 33 (2017) 1433–1447. https://doi.org/10.1016/j.jmst.2017.09.011.

[40] M. Isfandbod, E. Martínez-Pañeda, A mechanism-based multi-trap phase field model for hydrogen assisted fracture, Int. J. Plast. 144 (2021) 103044. https://doi.org/10.1016/j.ijplas.2021.103044.

[41] A.J. Kumnick, H.H. Johnson, Deep Trapping States for Hydrogen in deformed Iron, Acta Metall. 28 (1980) 33–39.

[42] A.H.M. Krom, A.D. Bakker, Hydrogen trapping models in steel, Metall. Mater. Trans. B Process

Metall. Mater. Process. Sci. 31 (2000) 1475–1482. https://doi.org/10.1007/s11663-000-0032-0.

[43] K. Kiuchi, R.B. McLellan, The solubility and diffusivity of hydrogen in well-annealed and deformed iron, Acta Metall. 31 (1983) 961–984. https://doi.org/10.1016/0001-6160(83)90192-X.

[44] E. Fallahmohammadi, F. Bolzoni, L. Lazzari, Measurement of lattice and apparent diffusion coefficient of hydrogen in X65 and F22 pipeline steels, Int. J. Hydrogen Energy. 38 (2013) 2531–2543. https://doi.org/10.1016/j.ijhydene.2012.11.059.

[45] L.B. Peral, A. Zafra, I. Fernández-Pariente, C. Rodríguez, J. Belzunce, Effect of internal hydrogen on the tensile properties of different CrMo(V) steel grades: Influence of vanadium addition on hydrogen trapping and diffusion, Int. J. Hydrogen Energy. 45 (2020) 22054–22079. https://doi.org/10.1016/j.ijhydene.2020.05.228.

[46] A. Zafra, L.B. Peral, J. Belzunce, Hydrogen diffusion and trapping in A 42CrMo4 quenched and tempered steel: Influence of tempering temperature, Int. J. Hydrogen Energy. 45 (2020) 31225–31242. https://doi.org/10.1016/j.ijhydene.2020.08.134.

[47] Y. Sakamoto, T. Mantani, Effect of quenching and tempering on diffusion of hydrogen in carbon steel, Trans. JIM. 17 (1976).

[48] F.G. Wei, K. Tsuzaki, Response of hydrogen trapping capability to microstructural change in tempered Fe-0.2C martensite, Scr. Mater. 52 (2005) 467–472. https://doi.org/10.1016/j.scriptamat.2004.11.008.

[49] S. Frappart, X. Feaugas, J. Creus, F. Thebault, L. Delattre, H. Marchebois, Study of the hydrogen diffusion and segregation into FeCMo martensitic HSLA steel using electrochemical permeation test, J. Phys. Chem. Solids. 71 (2010) 1467–1479. https://doi.org/10.1016/j.jpcs.2010.07.017.

[50] T. Si, Y. Liu, Q. Zhang, D. Liu, Y. Li, Effect of microstructure on hydrogen permeation in EA4T and 30CrNiMoV12 railway axle steels, Metals (Basel). 9 (2019). https://doi.org/10.3390/met9020164.

[51] T.L. Anderson, Fracture Mechanics. Fundamentals and applications, 4th ed., CRC Press, USA, 1991.

[52] G. Álvarez, A. Zafra, F.J. Belzunce, C. Rodríguez, Hydrogen embrittlement analysis in a CrMoV steel by means of sent specimens, Theor. Appl. Fract. Mech. 106 (2020) 102450. https://doi.org/10.1016/j.tafmec.2019.102450.